AFRL-AFOSR-UK-TR-2019-0022

Experimental Measurement of Fluidic Thrust Vectoring on Internal and External Expansion Hypersonic Nozzles

Andrew Neely
University of New South Wales-NEW NCAGE Code
HIGH STREET
KENSINGTON, NSW, 2052
AU

05/09/2019
Final Report

Air Force Research Laboratory
Air Force Office of Scientific Research
European Office of Aerospace Research and Development
Unit 4515 Box 14, APO AE 09421

REPORT DOCUMENTATION PAGE

Form Approved
OMB No. 0704-0188

The public reporting burden for this collection of information is estimated to average 1 hour per response, including the time for reviewing instructions, searching existing data sources, gathering and maintaining the data needed, and completing and reviewing the collection of information. Send comments regarding this burden estimate or any other aspect of this collection of information, including suggestions for reducing the burden, to Department of Defense, Executive Services, Directorate (0704-0188). Respondents should be aware that notwithstanding any other provision of law, no person shall be subject to any penalty for failing to comply with a collection of information if it does not display a currently valid OMB control number.
PLEASE DO NOT RETURN YOUR FORM TO THE ABOVE ORGANIZATION.

1. REPORT DATE *(DD-MM-YYYY)*	2. REPORT TYPE	3. DATES COVERED *(From - To)*
09-05-2019	Final	30 Sep 2017 to 29 Sep 2018

4. TITLE AND SUBTITLE
Experimental Measurement of Fluidic Thrust Vectoring on Internal and External Expansion Hypersonic Nozzles

5a. CONTRACT NUMBER

5b. GRANT NUMBER
FA9550-17-1-0401

5c. PROGRAM ELEMENT NUMBER
61102F

6. AUTHOR(S)
Andrew Neely

5d. PROJECT NUMBER

5e. TASK NUMBER

5f. WORK UNIT NUMBER

7. PERFORMING ORGANIZATION NAME(S) AND ADDRESS(ES)
University of New South Wales-NEW NCAGE Code
HIGH STREET
KENSINGTON, NSW, 2052 AU

8. PERFORMING ORGANIZATION REPORT NUMBER

9. SPONSORING/MONITORING AGENCY NAME(S) AND ADDRESS(ES)
EOARD
Unit 4515
APO AE 09421-4515

10. SPONSOR/MONITOR'S ACRONYM(S)
AFRL/AFOSR IOE

11. SPONSOR/MONITOR'S REPORT NUMBER(S)
AFRL-AFOSR-UK-TR-2019-0022

12. DISTRIBUTION/AVAILABILITY STATEMENT
A DISTRIBUTION UNLIMITED: PB Public Release

13. SUPPLEMENTARY NOTES

14. ABSTRACT
This interim Final Report presents the results of a 1-year project to design and demonstrate experimental methods to measure the performance of fluidic thrust vectoring on internal and external expansion hypersonic nozzles. A numerical study of both configurations is reported. Experimental measurements for the external expansion nozzle are also reported. The final phase of the project, repeating the experiments for the internal expansion nozzle, will be completed in early 2019.

15. SUBJECT TERMS
hypersonic, fluidic control, nozzles

16. SECURITY CLASSIFICATION OF:			17. LIMITATION OF ABSTRACT	18. NUMBER OF PAGES	19a. NAME OF RESPONSIBLE PERSON
a. REPORT	b. ABSTRACT	c. THIS PAGE			SMITH, DOUGLAS
Unclassified	Unclassified	Unclassified	SAR		**19b. TELEPHONE NUMBER** *(Include area code)* 314-235-6013

Standard Form 298 (Rev. 8/98)
Prescribed by ANSI Std. Z39.18

Experimental measurement of fluidic thrust vectoring on internal and external expansion hypersonic nozzles

Grant Number: **FA9550-17-1-0401**

Interim
Final Report

Andrew Neely (UNSW), Matthew McGilvray, (Oxford), Luke Doherty (Oxford), Jouke de Baar (UNSW)

Collaborators: William Iveson (Oxford), Chris Hambidge (Oxford), Tobias Hermann (Oxford), David Steuer (Stuttgart), Hilbert van Pelt (UNSW)

29 December, 2018

v1.1 Dec 2018

Experimental measurement of fluidic thrust vectoring on internal and external expansion hypersonic nozzles

Andrew Neely (UNSW), Matthew McGilvray, (Oxford), Luke Doherty (Oxford),
Jouke de Baar (UNSW)

Collaborators: William Iveson (Oxford), Chris Hambidge (Oxford), Tobias Hermann (Oxford), David Steuer (Stuttgart), Hilbert van Pelt (UNSW)

20 December, 2018

Abstract

This interim Final Report presents the results of a 1-year project to design and demonstrate experimental methods to measure the performance of fluidic thrust vectoring on internal and external expansion hypersonic nozzles. A numerical study of both configurations is reported. Experimental measurements for the external expansion nozzle are also reported. The final phase of the project, repeating the experiments for the internal expansion nozzle, will be completed in early 2019.

Motivation

Hypersonic vehicles require fast response aerodynamic control with sufficient control authority. Existing techniques rely on aerodynamic control surfaces (Skujins 2010) that increase mass and drag and suffer from extreme thermal-structural heating (Van Wie *et al.* 2004). Fluidic thrust vectoring (FTV) employs the injection of a secondary flow into the nozzle exit flow to steer the exhaust and thus vector the thrust (Figure 1). This can potentially be achieved at significantly lower mass and complexity than mechanical thrust vectoring systems. More efficient scramjet designs may therefore be possible using FTV, that reduce or even eliminate the need for these aerodynamic control surfaces.

It has been shown that reaction control thrusters exhausting into a hypersonic cross flow can result in useful amplification of the momentum thrust (Spaid 1975, Brandeis & Gill 1996, 1998). Other studies have examined the use of magnetohydrodynamics for this same purpose (Shneider & Macheret 2005, Macheret *et al.* 2004) but these systems are also unproven and are likely to require more dedicated on-board hardware and thus be significantly heavier than an FTV system.
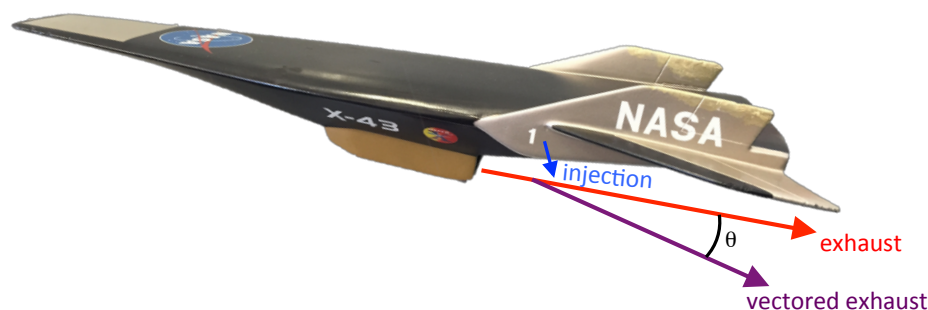

Figure 1. FTV on a hypersonic vehicle

A growing body of work (e.g. Berens 1993, Sellam *et al.* 2015), including that undertaken at UNSW Canberra by the CI (Neely *et al.* 2007, Ali *et al.* 2012, Bright *et al.* 2014, van Pelt *et al.* 2015), has examined the application of FTV to a range of nozzle geometries, particularly rockets and gas turbine nozzles, but the experimental work has all been into a quiescent, ambient air (e.g. Figure 2). Those studies that have been performed on scramjet exhausts have been purely numerical. In the application of FTV to scramjet nozzles, the interaction between the exhaust flow from the nozzle and the injected secondary flow will be subject to a further interaction with the hypersonic freestream, which must be

investigated to quantify its effect on the FTV. This study extends a pilot study, recently funded at UNSW ($20k) to establish an experimental methodology to perform experiments on FTV nozzles in a hypersonic cross flow. The initial proof of concept study was performed in Australia in the first half of 2017 and was limited to 15 shots and to a single, non-optimised external expansion nozzle geometry at Mach 5.8. Due to manufacturing constraints, only a simple single (almost) full width slot injector was used. The current project, described in this report, with experiments undertaken in the High Density Tunnel at the University of Oxford, has continued this work by evolving the design of the model and its instrumentation to incorporate a more complex supersonic nozzle injector arrangement. This new work more comprehensively characterises the flow field and compares the fluid dynamics and performance in both generic external and internal compression nozzles.
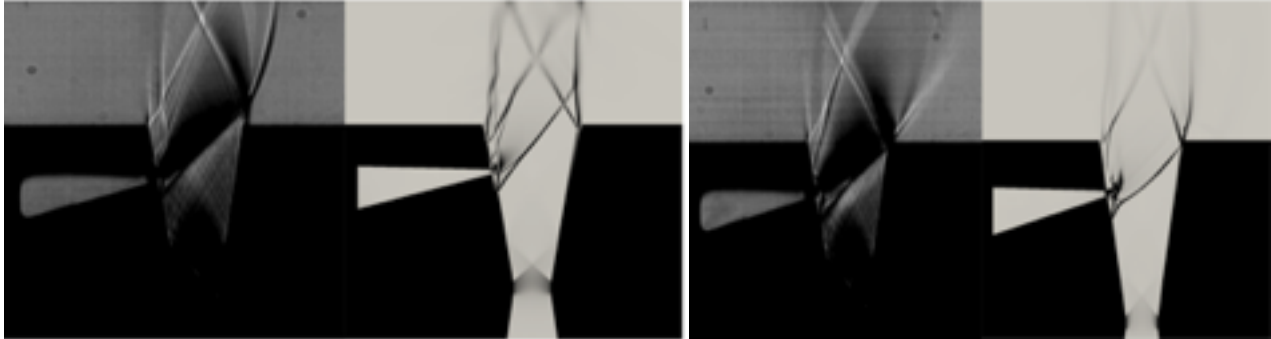

Figure 2. Testing a 2D FTV nozzle in the UNSW supersonic nozzle rig, expansion into quiescent ambient air. (a) 20 bar supply pressure, 4 bar injection pressure; (b) 20 bar supply pressure, 8 bar injection pressure.
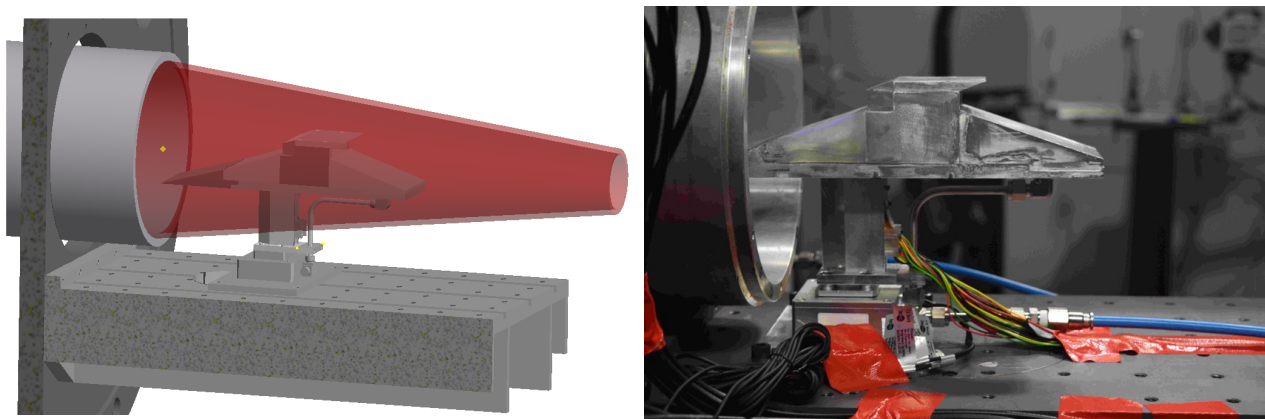

Figure 3. Layout of the original scramjet FTV experiments performed in the TUSQ facility by van Pelt (2018) showing (a) a CAD image of the model within the nozzle exit flow core and (b) a photo of the instrumented model in the test section.

Aims

Experimentally measure the relative side force produced by an external thruster, and FTV on generic internal and external expansion nozzles. Comparison of these three cases will enable assessment of the relative performance for the given configurations and the accuracy of analytical models based on blast theory in predicting the side force.

Significance

This project continues the first published experimental investigation of FTV on a scramjet configuration. It measures the control forces on FTV equipped external and internal expansion nozzles in representative hypersonic cross flow conditions. It establishes an experimental methodology to determine the interaction of the injectant with the core exhaust flow and the hypersonic freestream flow and measure the influence of an external expansion nozzle (Gu *et al.* 2011) with FTV on control authority. Both internal and external expansion nozzles have been employed in the design of scramjet powered vehicles including NASA's X-43 (Figure 4) and the USAF's X-51 (Figure 5) respectively.
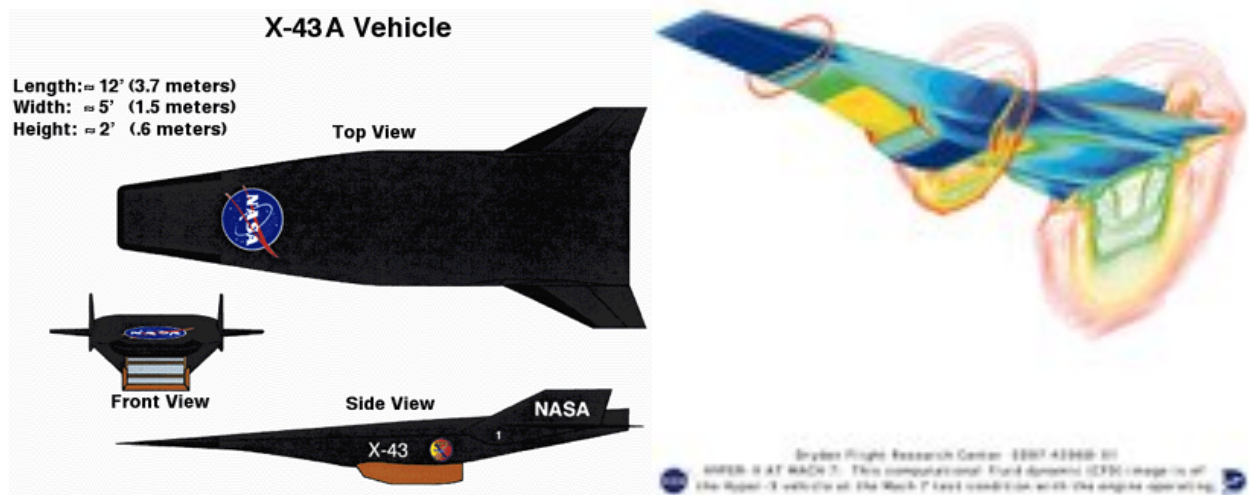
Figure 4. Figure 4. External expansion nozzle on the X-43 Hyper-X vehicle. (NASA).

Figure 5. Internal expansion nozzle on the X-51 waverider (Dahm 2010)

Numerical study of FTV performance in internal and external expansion nozzles

To provide design and validation data for the experiments, 2D CFD simulations were performed on four different geometric model configurations that combined upstream and downstream injector locations with the internal and external nozzle designs incorporating different length cowls. The two-dimensional geometry of the scramjet model is shown in Figure 6 for the external expansion nozzle configuration. The internal expansion nozzle configuration simply extends the cowl a further 98.2 mm to the end of the model. The wind tunnel model adds 5 mm sidewalls extending from the leading edge to the trailing edge of the cowl.
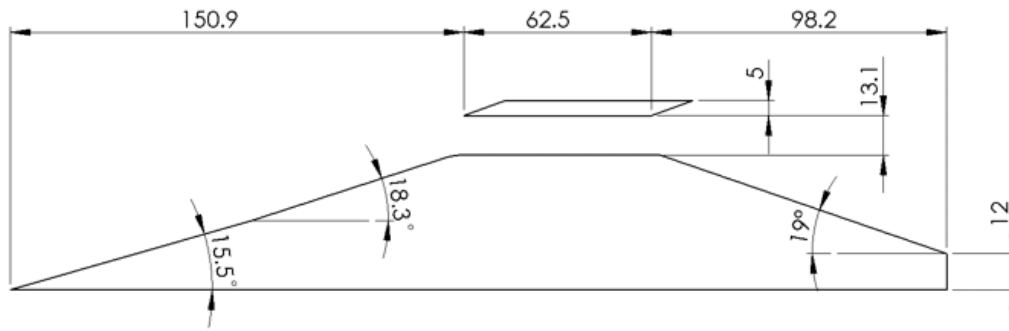
3

Figure 6. Dimensions of model (in mm) with external expansion nozzle. For the internal expansion nozzle, the cowl is lengthened a further 98.2 mm to the rear of the model.

The simulations were performed using the ANSYS Fluent solver (v18.2). The k-ω SST turbulence model was chosen for its ability to resolve adverse pressure gradients, to predict flow separation, and its suitability to simulate internal flows (e.g. Ali *et al.* 2012, Bright *et al.* 2014). The boundary conditions were set to the nominal experimental freestream conditions, which were, in Figure 8, $p_0 = 13$ and 21.5 bar and $T_0 = 460$ K at a Mach number of 6. This resulted in freestream unit Reynolds numbers of 18.57 and 20.89 $\times 10^6$ m^{-1}. The pressure of the injected gas was stepped from 0 kPa to 120 kPa. The forces and moments from this analysis were used in the sizing of the chosen load cell as well as for the dimensioning of the mounting for the experiment.

The initial 2D CFD simulations were performed for both upstream and downstream injector locations using a supersonic slot injectors. As pitch moment is the desired control output, locating the injectors as far downstream of the vehicle CoG is advantageous.
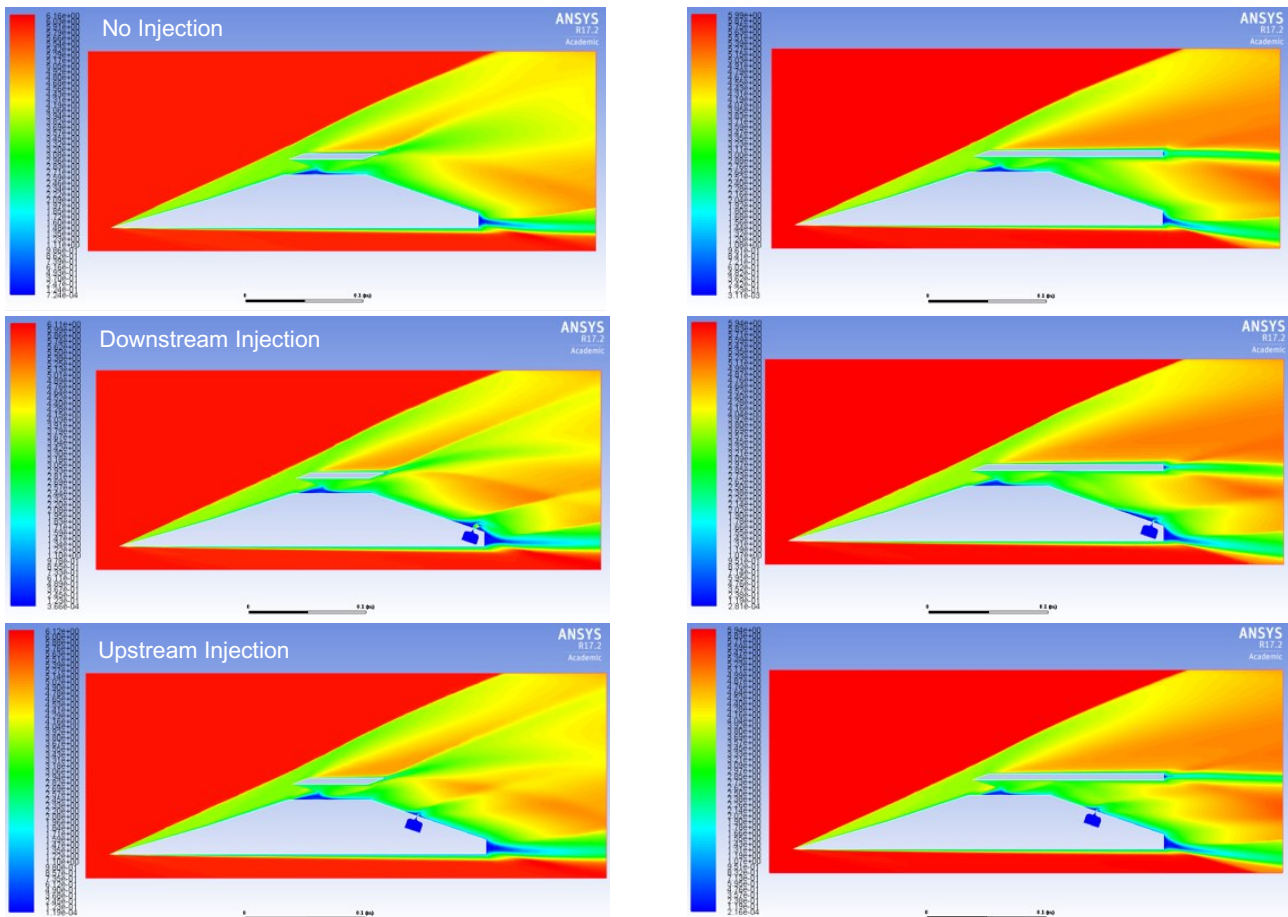

Figure 7. 2D CFD steady state simulations of the Mach number distributions in the flow field for (a) no injection, (b) downstream injection and (c) upstream injection for both the external and internal nozzle configurations.

4

Table 1 compares the component and net forces and moments on the model from the 2D CFD simulations shown in Figure 7. The 2D results have been approximated to the 3D case by multiplying the values calculated per metre width by the width of the test model (0.08 m). As expected the net change in moment generated by the activated FTV system is greater for the downstream injector than the upstream injector. Interestingly the increase in pitching moments are greater when FTV is employed on the external expansion nozzle as compared with the case for the internal expansion nozzle.

While Spaid (1975) found little influence of the crossflow Mach number and injector position on the amplification factor for his experiments on injection from a flat plate, it should be noted that he was (a) only using sonic injectors and (b) injecting into a non-expanding flow. Wu *et al.* (1961), in a study on injection into a conical nozzle, demonstrated the additional effects of the injection Mach number and the resultant Mach number ratio, that is itself dependent on the expansion in the nozzle and thus where the injectors are located in a nozzle. This all leads to a greater side force (and not just moment) for downstream injectors. This is borne out slightly from the predicted forces reported in Table 1.

Table 1. Comparison of component and net forces and moments from 2D CFD simulations shown in Figure 7.

EXTERNAL EXPANSION NOZZLE

No Injection				Downstream Injection				Upstream Injection		
Zone	Fx [N]	Fy [N]	Mz(0,0) [Nm]	Zone	Fx [N]	Fy [N]	Mz(0,0) [Nm]	Zone	Fx [N]	Fy [N]	Mz(0,0) [Nm]
front	336.84	-1039.39	-86.04	front	338.59	-1039.28	-85.94	front	337.7	-1037.5	-85.8
top	6.61	-721.88	-137.63	top	5.93	-774.56	-147.22	top	6.3	-798.3	-151.7
back	-57.86	-175.45	-42.06	back	-68.16	-194.56	-47.19	back	-66.9	-193.3	-46.0
bottom	9.31	330.74	50.56	bottom	10.29	332.96	50.97	bottom	10.4	333.4	51.1
cowl	64.65	895.44	150.92	cowl	67.62	915.17	153.77	cowl	68.7	936.7	157.5
Net	359.55	-710.54	-64.25	Net	354.28	-760.26	-75.61	Net	356.1	-759.0	-74.9
Net*0.08	28.76	-56.84	-5.14	Net*0.08	28.34	-60.82	-6.05	Net*0.08	28.5	-60.7	-6.0
				delta	0.42	3.98	0.91	delta	0.28	3.88	0.85

INTERNAL EXPANSION NOZZLE

No Injection				Downstream Injection				Upstream Injection		
Zone	Fx [N]	Fy [N]	Mz(0,0) [Nm]	Zone	Fx [N]	Fy [N]	Mz(0,0) [Nm]	Zone	Fx [N]	Fy [N]	Mz(0,0) [Nm]
front	337.19	-1039.90	-86.12	front	336.62	-1036.47	-85.71	front	337.5	-1038.4	-85.9
top	6.68	-730.75	-139.22	top	6.06	-752.03	-143.16	top	6.6	-1129.7	-132.0
back	-72.62	-214.94	-53.29	back	-88.42	-239.72	-60.20	back	-79.0	-218.0	-54.7
bottom	9.36	330.79	50.59	bottom	9.75	331.74	50.79	bottom	10.0	329.5	50.3
cowl	79.40	1414.68	276.64	cowl	81.90	1422.05	277.99	cowl	81.2	1351.2	264.2
Net	360.01	-240.11	48.60	Net	345.91	-274.44	39.72	Net	356.4	-705.4	41.8
Net*0.08	28.80	-19.21	3.89	Net*0.08	27.67	-21.95	3.18	Net*0.08	28.5	-56.4	3.3
				delta	1.13	2.75	0.71	delta	0.29	37.22	0.54

The CFD provided a prediction of the flow field over the model and around the injector slot. The results are self-consistent, with an increase in deflection of the main flow and larger separations of the upstream boundary layer at higher injection pressure ratios. The results showed a similar behaviour for the second set of simulations undertaken at a higher tunnel fill pressure of 21.5 bar, though the deflection is smaller for a given injection total pressure. After the testing it could be seen that the CFD tended to over-predict the resulting forces as well as the size of the boundary layer separation in comparison to the experimental results. This is expected as the simulations were performed in 2D, and they did not account for the limited width of the injector array or allow for flow spillage over the sides of the model. However, the overall simulated behaviour of FTV was consistent with the experimental data. The extent of the injected gas (N_2) is also presented in Figure 9 as mole fraction. The majority of this gas flows directly away from the model and out of the rear boundary of the simulation, but a small amount back-fills the separated volume. However, this does not reach the upstream shock location.
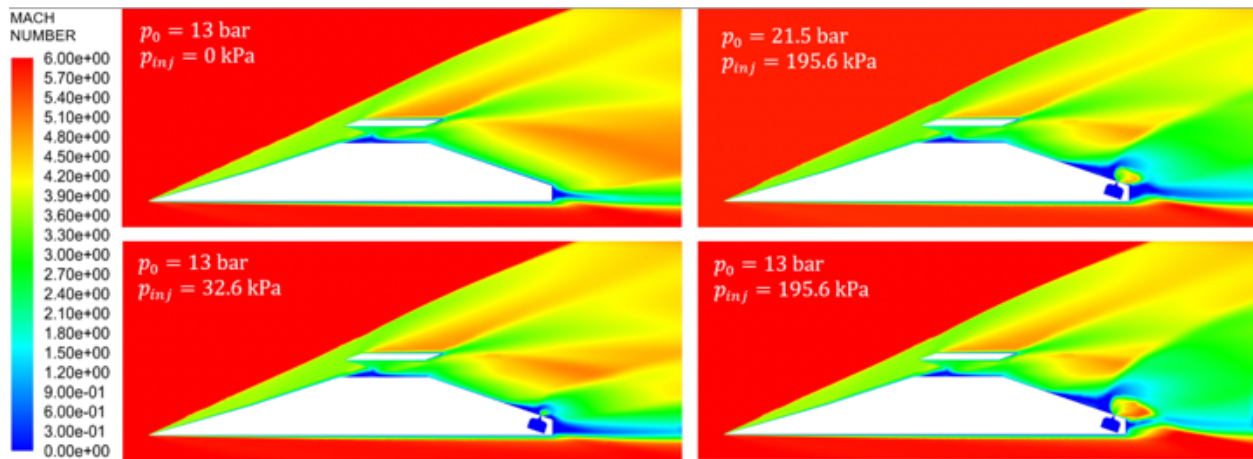
Figure 8. Comparison of Mach number distribution for simulations performed on the external expansion nozzle configuration at different injection pressures, total freestream pressure and total injection pressure as indicated.
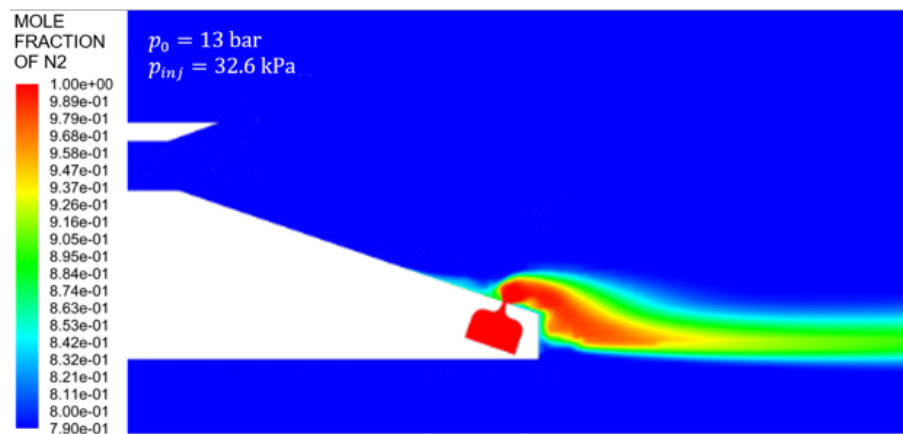

Figure 9. Detail of CFD simulation of injection of N_2 into a crossflow of air for comparison with the PSP injection footprint studies.

Wind Tunnel Model Design

The experimental model was designed as a 2D generic scramjet shape, following a similar geometry to van Pelt *et al.* (2017). The two ramp intake compresses the freestream flow before expanding it through a 19° straight-sided nozzle (Figure 10). For the initial experiments in the Oxford HDT, the injector was located at the end of the exhaust on the body side to maximise the moment arm and the penetration into the expanded cross flow. Figure 11 shows CAD images of the model, where the model is 311.6 mm long and 80 mm wide. This configuration thus formed a 2D generic analogue of an external expansion scramjet nozzle like that used on the NASA X-43 (McClinton 2016), although the actual geometry was two-dimensionalised and the intake and nozzle angles were adjusted to suit the Mach 6 free-stream condition in the HDT.
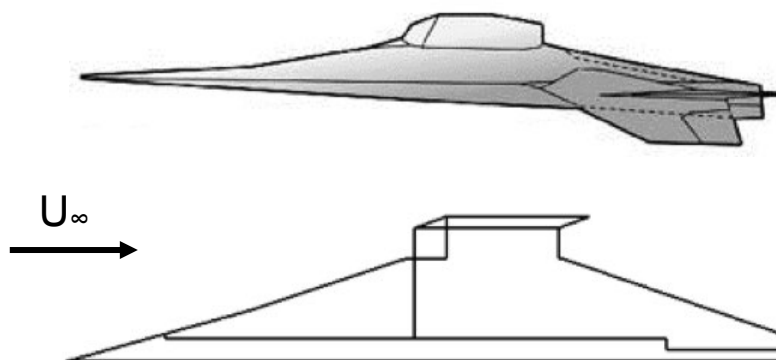

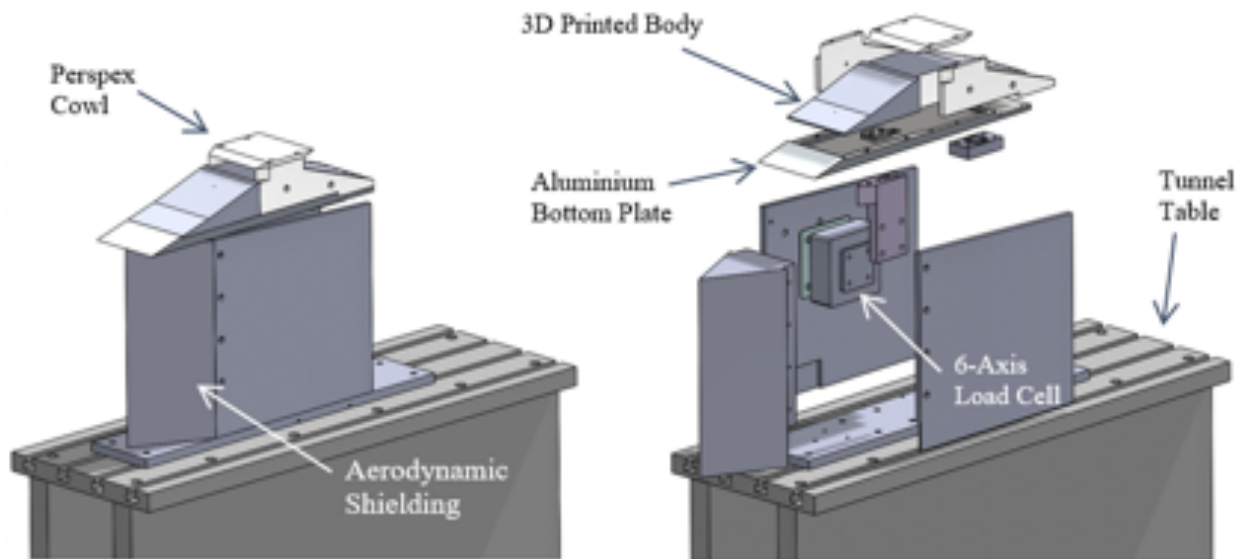Figure 10. the NASA X-43 (McClinton 2016) compared with the design used in this project, flow direction indicated

Figure 11. Assembled and exploded CAD images of the FTV wind tunnel model, in the external expansion nozzle configuration, showing detail of the flow shielding around the load cell and model support.

Measurements were taken of surface pressure along the body, injection pressure and temperature, and loads and moments on the model. A commercial Tecsis F9866 six-component load cell (tecsis.com) was used to measure the forces and moments on the model for both injection-on and -off conditions. The injection-off measurements were used to baseline the net forces and moments for the FTV. The load cell had a full range of 200 N and 6 Nm and had a nominal bandwidth of 2 kHz. The moment arm used was 145 mm downstream and 61 mm below the leading edge of the model.
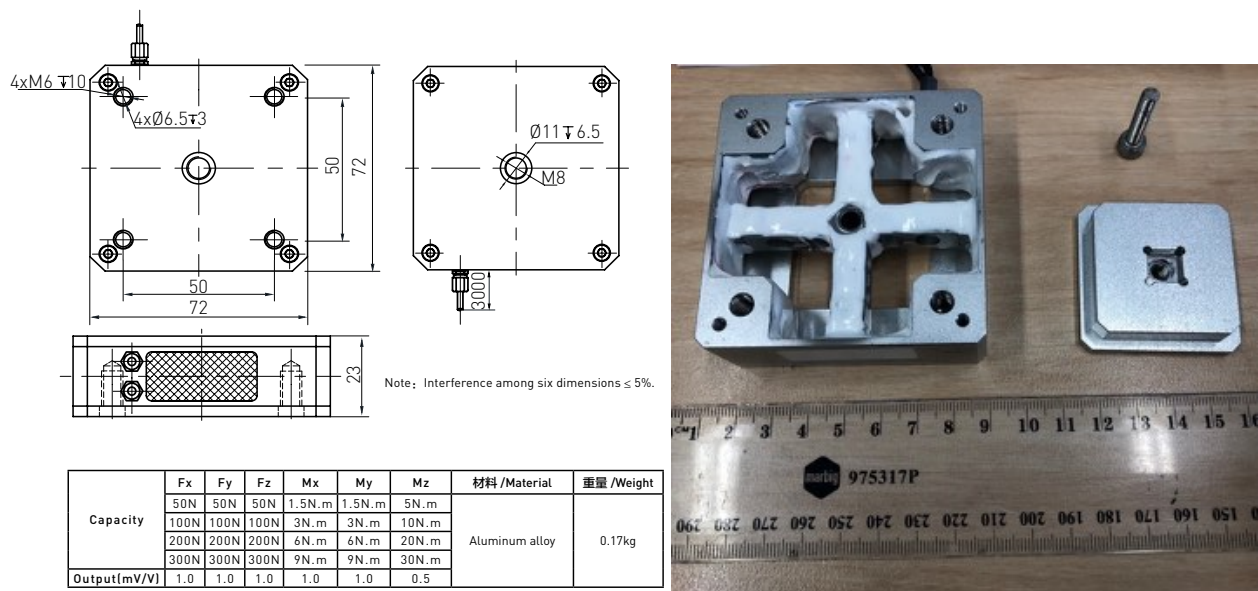

	Fx	Fy	Fz	Mx	My	Mz	材料 /Material	重量 /Weight
Capacity	50N	50N	50N	1.5N.m	1.5N.m	5N.m		
	100N	100N	100N	3N.m	3N.m	10N.m		
	200N	200N	200N	6N.m	6N.m	20N.m	Aluminum alloy	0.17kg
	300N	300N	300N	9N.m	9N.m	30N.m		
Output(mV/V)	1.0	1.0	1.0	1.0	1.0	0.5		

Figure 12. (a) Geometry and capacity of the commercial Tecsis F9866 six-component load cell. (b) disassembled load cell showing instrumented cruciform and attachment plate.

The initial model design used in these experiments followed the approach of van Pelt *et al.* (2017), used in the TUSQ facility at the University of Southern Queensland in Australia, by mounting the model vertically above load cell using a stiff support arm to connect the model to the horizontally mounted load cell. Unlike the arrangement in TUSQ in which the support arm incorporated a sharp leading edge and was directly exposed to the test flow, the model designed and manufactured for the Oxford HDT used a large, rigid shield to protect the support arm and the load cell from aerodynamic loading by the flow (Figure 13). The difference in the relative positions of the nozzle centreline and the model support bed between TUSQ and the HDT, however, resulted in a significant increase in the length of the support arm. This in turn exacerbated the problem originally observed by van Pelt *et al.* (2017) of the model rocking backwards during the run due to the compliance of the load cell, varying the angle of attack of the model during the experiment. The side shield plates had to be modified to accommodate this rocking and prevent unwanted contact between the free-floating model and the shields in the initial pass-off testing in the HDT.
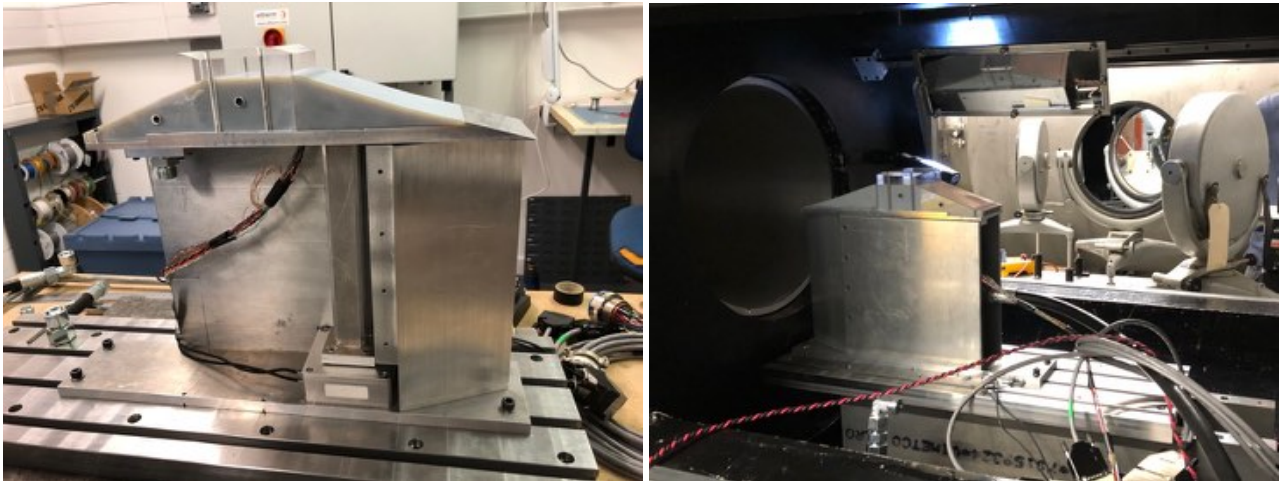
Figure 13. Photos showing the initial model configuration used in the Oxford HDT incorporating the long support arm joining the free floating model to the six-component load cell.

For the comprehensive test campaigns, the model was modified by significantly shortening the support, and thus the moment arm and attaching it to the six-component load cell which was mounted directly to the inside of the flow shield (Figure 11). The orientation of the load cell was changed to the vertical axis thus also reducing the compliance of the load cell. These modifications together served to reduce the rocking of the model during the experiments sufficiently to not influence the measurements.

The injector was slot like (Figure 14), and contained a transverse array of six, closely-spaced, individual converging diverging supersonic nozzles which were choked to ensure the mass flow rate was independent of the local freestream. The nozzles had a total throat area of 25.2 mm^2 and an exit area of 42 mm^2, giving a nominal exit Mach number of 2. The manufactured slot injectors are shown in Figure 15. Calibration of the injector nozzles measured a discharge coefficient of 0.81.
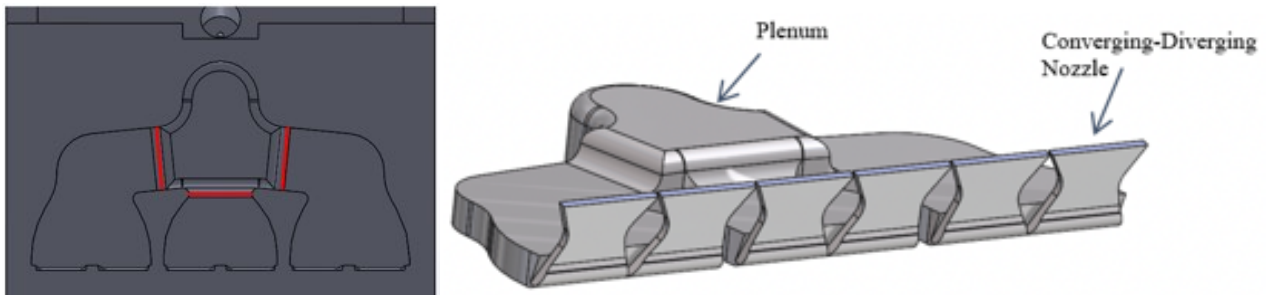

Figure 14. CAD images showing detail of the injector plenum and 3 pairs of supersonic injector nozzles in the 3D printed model.
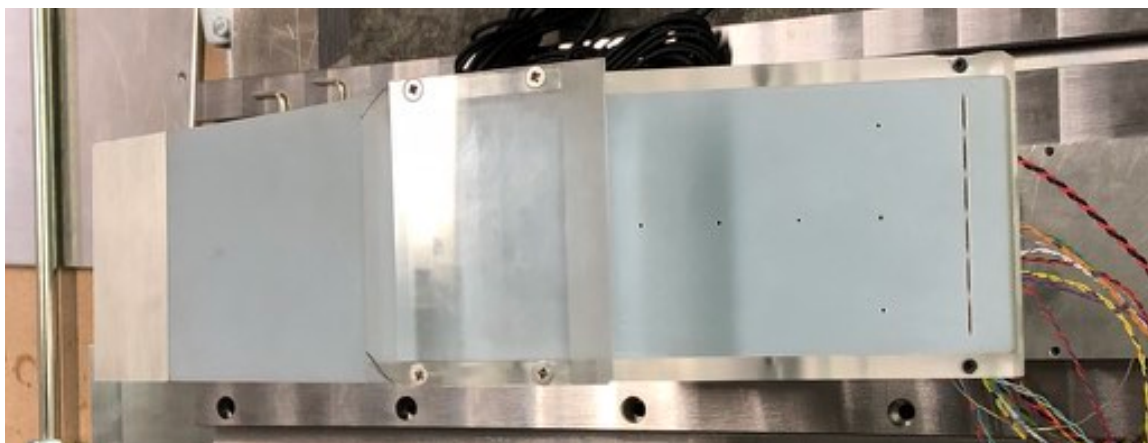

Figure 15. Photo of the upper surface of the model showing the relative positions of the slot injectors and the pressure tappings on the nozzle surface.

The geometry of the injection system was simulated using CFD. A 3-dimensional solution was obtained to investigate the velocity profile along the length of the injection slot. Figure 16 presents the results from this simulation showing that the manufactured injection geometry successfully produces an injection with a fairly even velocity profile along its width. The flow simulated here injects into a vacuum so the results don't incorporate the effects of cross flow on the flow structure like that experienced in the experimental tests.

a) A view of the nozzle cross-section with approximate locations of view b) (vertical) and view c) (horizontal)

b) A side view

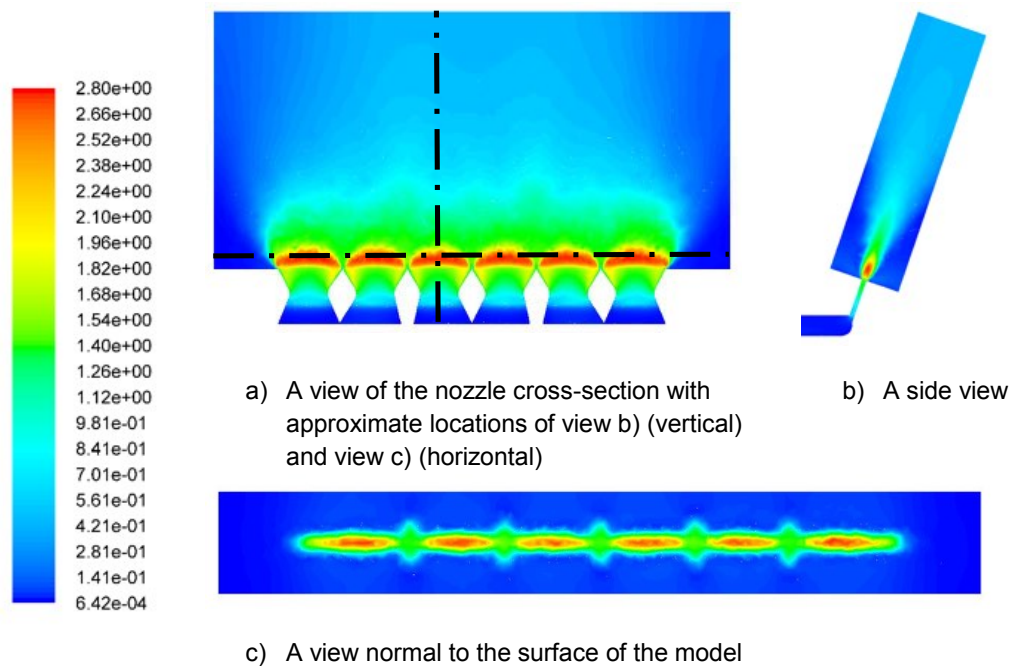c) A view normal to the surface of the model

Figure 16. Contours of Mach number for the injection geometry – 20 kPa into a vacuum.

Figure 17 shows a photograph of the instrumentation mounted internally within the model. The intake and nozzle block portions of the model were manufactured as a single piece using a Stratasys Objet30 Pro 3D printer to enable the complex internal geometry of the injectors and supply plenums to be produced at low manufacturing cost. This plastic block was mounted into an aluminium body to form the scramjet geometry which was in turn mounted on the aluminium support member.

Honeywell SDX15A2 pressure transducers were connected to the model at locations along the centreline of the body and laterally slightly upstream of the injector. These were joined to the surface with flexible tubes less than 50 mm long to minimise response times. Additionally, one was connected to the plenum of the injection system. All pressure transducers were directly connected to the DAQ. These were calibrated whilst pumping down the test section using an Inficon CDG025D high precision vacuum gauge.

Flow field visualisation was obtained using high-speed video schlieren. All pressure transducers and thermocouples were recorded using an NI PXIe-8135 controller with NI PXIe-6368 acquisition cards at 200 kS/s/channel. Timings for the cameras were set through the digital acquisition system (DAQ), which was triggered off the rise in tunnel stagnation pressure with a pre-trigger time of 300 ms.
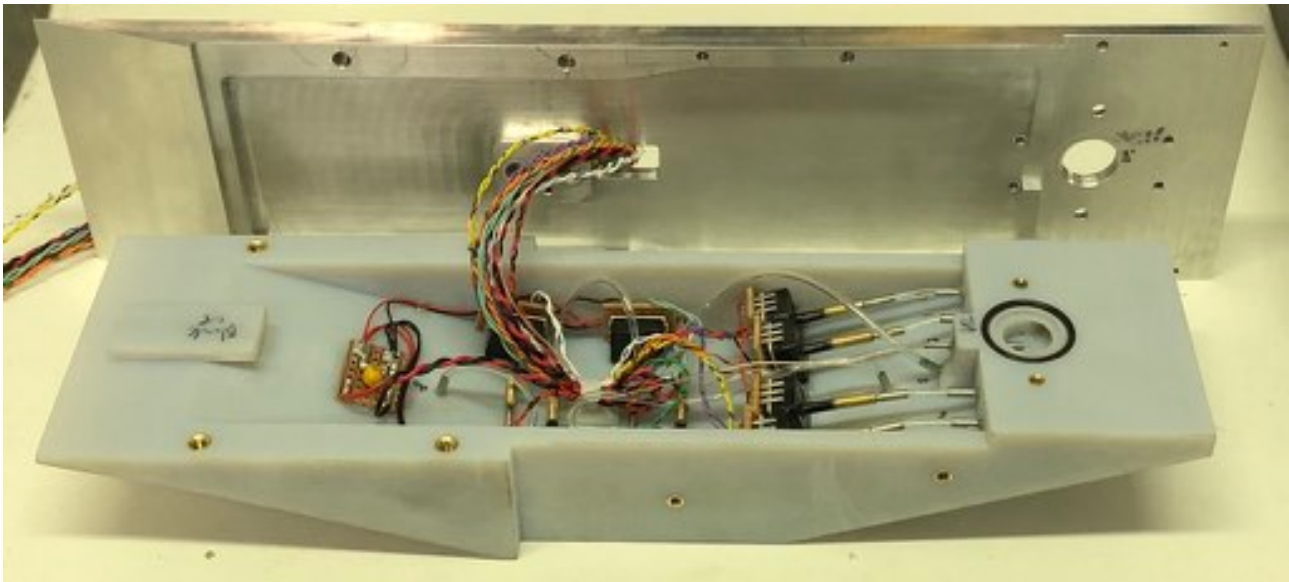
Figure 17. Detailed view of the pressure and thermocouple instrumentation within the cavity of the 3D printed plastic model. The aluminium base is also shown as is the gas feed to the internal plenum chamber.

A 0.25 mm diameter butt-welded K-type thermocouple was mounted into the middle of the entrance pipe to the injector plenum (Figure 17). Flow speeds here were estimated to be 95 m/s, which gives a slow response to the thermocouple, estimated to be 1 ms. However, the start-up transients are observed to become steady within the test period. The thermocouple was amplified with a FYLDE FE-351-UA, with a gain of 1000.

Each channel of the load cell was amplified using a FYLDE FE-H379-TA set in a full bridge mode with a 30 kHz low pass filter and had a gain of 1000. The load cell was statically calibrated using dead weights. The raw force and moment readings from the load cell exhibited a significant amount of noise at two specific frequencies. Therefore, two notch filters were used in series: the first centred on 100 Hz and the second centred on 5 kHz.

To measure the distribution of pressure across the nozzle and enable visualisation of the footprint of the separation interaction at the injectors, ISSI FP Porous, Fast Response Pressure Sensitive Paint (PSP) was applied to the wetted surface of the nozzle. This was calibrated in the same manner as the pressure transducers. The PSP was illuminated from directly above with a Luminux CBT-180 UV LED at 24 V (Willert *et al.* 2010) mounted to support rails on the ceiling of the test section, with a diffuser placed in front of it. The surface was imaged via a mirror onto a Photron Mini-UX 200 at a frame rate of 10 kfps and used a red notch filter in front of the lens. The images were transformed frame-by-frame using edge detection back to cartesian co-ordinates which compensated for model motions due to vibration. This applied the data processing techniques detailed in Hermann *et al.* (2018).

Experimental Set up

Testing took place in the Oxford High Density Tunnel (HDT), operated as a heated Ludwieg Tunnel (Figure 18). The facility features a 152 mm diameter, 17.3 m length barrel that can be pre-heated up to 550 K, which allows the high pressure test gas to be expanded to hypersonic Mach numbers while avoiding liquefaction. A Mach 6 contoured nozzle with an exit diameter of 350 mm was used. The initial fill conditions are set to meet the desired stagnation pressure and temperature in the test, which are directly measured. The facility produces up to five plateaus of steady flow of approximately 30 ms each, set by the plug opening time and the transit of the unsteady expansion waves along the facility. A particular benefit of this facility for FTV work is the range of test conditions that can be achieved and sufficient test times to allow the use of a traditional load cell. In contrast, shock tunnels, with durations of order 1 ms, would require a more complex methodology (Mee *et al.* 1996).
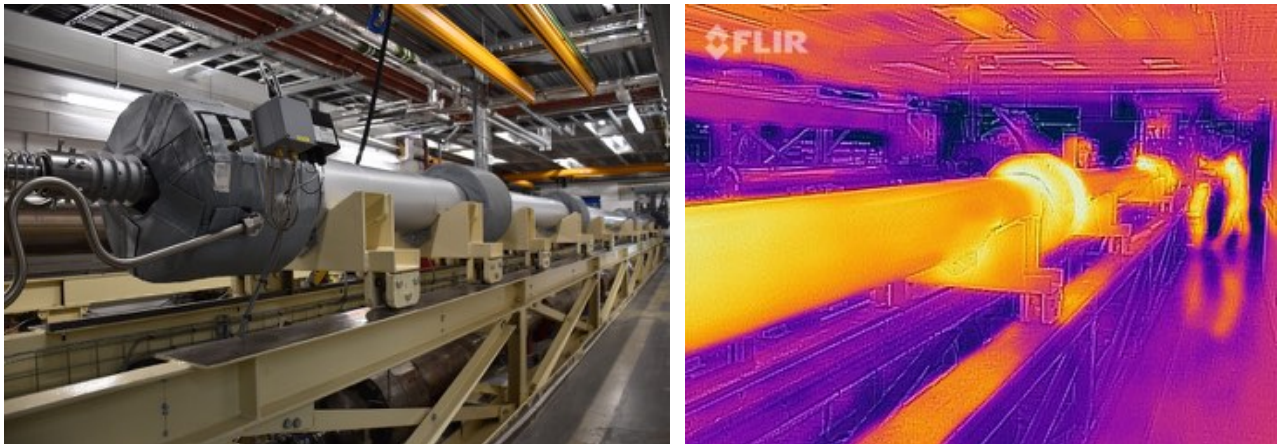
Figure 18. Photograph of the Oxford University High Density Tunnel (HDT), looking downstream with an IR thermograph showing the tunnel in heated mode.

The model was mounted in the test section at the exit of the Mach 6 nozzle (Figure 19) with the shielding and support rigidly bolted to the test section floor and located in view of the side windows. A mirror was mounted above and behind the model, outside of the test flow to enable imaging of the PSP response on the surface of the model (Figure 13, Figure 19).

A 108 mm diameter high speed Z-type schlieren system was setup for the experiments. This used a Luminux CBT- 180 green LED, with optics to clean up the light source (see Hermann *et al.* 2018 for details). A Photron Mini AX-100 video camera was used to video the flow field at 1280×1000 pixels, and a frame rate of 5 kfps. In addition to providing information about the flow field, this was also used to determine the injection-induced separation distance on the nozzle.
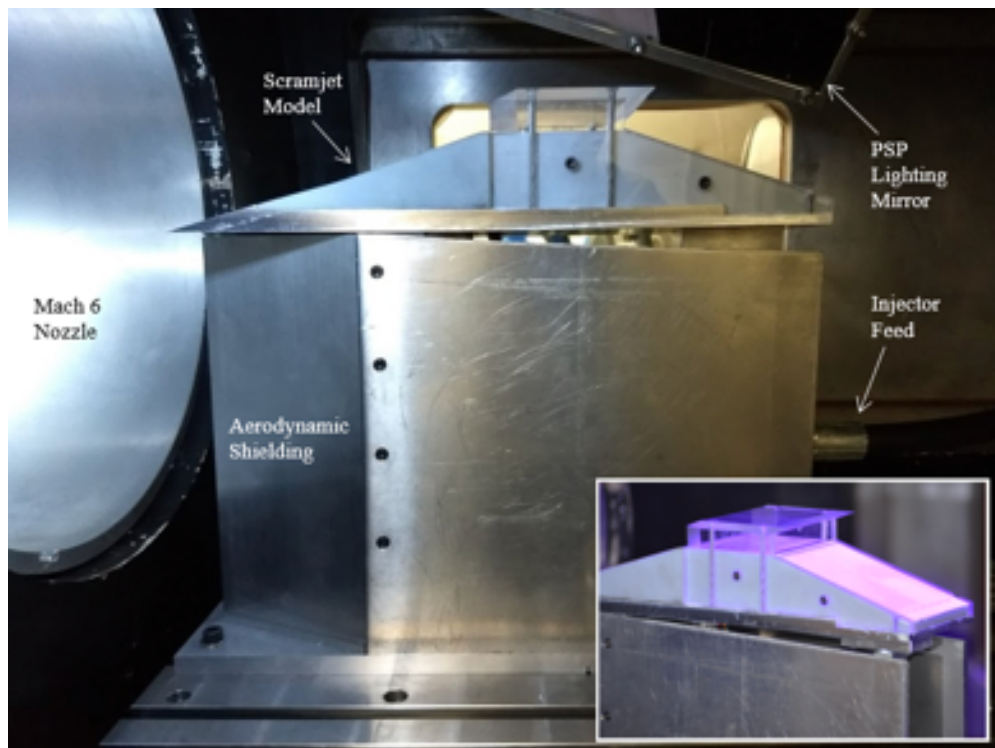

Figure 19. Photograph of the FTV model as installed in the Oxford High Density Tunnel. Illuminated PSP coated nozzle expansion surface (inset).

To enable injection of a control flow, a new gas injection system was implemented in the HDT. This consisted of a 4.9×10^{-3} m^3 external reservoir, which was connected through valve V5 (Figure 20) with 8 mm internal diameter pipework to the test section. The fast-acting valve had a minimum differential opening pressure of 0.7 bar. A limiter could be included to cause a pressure loss which enabled low pressures to be reached in the plenum. This system was controlled

via the tunnel control system to executed prescribed valve opening and closing times in relation to the tunnel operating sequence. Timings were set so that the pressure in the model's plenum reached a steady level before the tunnel was fired. The drop in plenum pressure over each test was < 1%.
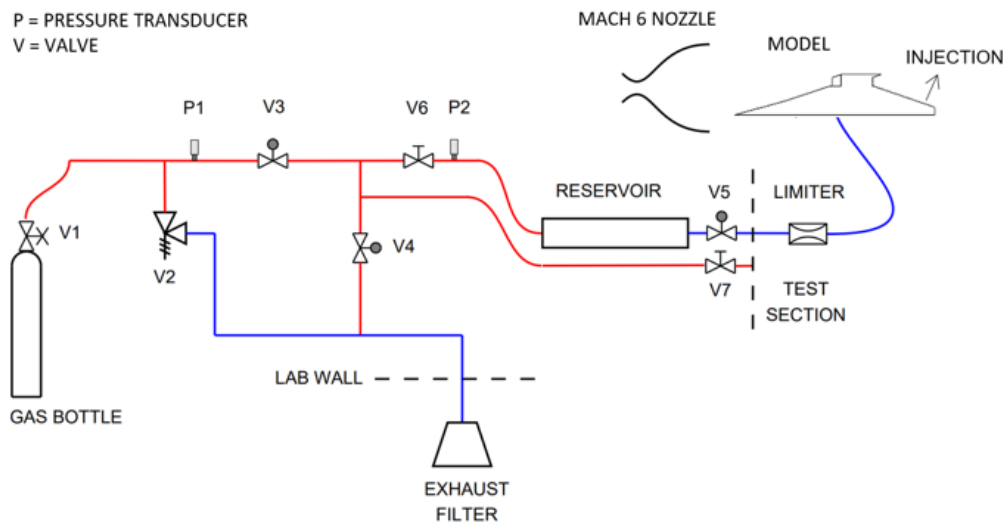

Figure 20. Schematic of the system used in the HDT to supply gas to the FTV injectors on the model.

Wind Tunnel Testing

The freestream conditions produced for the testing are detailed in Table 2. These values were calculated assuming isentropic expansion of air through the nozzle, using the measured stagnation pressure averaged over 30 ms and calibrated Mach number and total temperature. The viscosity was calculated via the Keyes relation (1952).

Table 2. Nominal flow properties for each condition which was tested in the HDT.

Con-dition	Mach number	Velocity (m/s)	Density (g/m^3)	Static pressure (Pa)	Static temperature (K)	Total pressure (MPa)	Total temperature (K)	Viscosity (Pa.s)	$\mathbf{Re}_{unit}$ (10^6/m)
1	6	823	87.0	1172	47.0	1.85	385.0	3.30×10^{-6}	21.7
2	6	822	75.4	1013	46.8	1.60	383.7	3.45×10^{-6}	18.0
3	6	821	66.2	887	46.7	1.40	382.6	3.29×10^{-6}	16.5
4	6	819	53.1	709	46.5	1.21	381.6	3.04×10^{-6}	14.3
5	6	823	61.1	823	47.0	1.30	385.0	3.81×10^{-6}	13.2
6	6	822	53.3	716	46.8	1.13	383.7	3.81×10^{-6}	11.5
7	6	821	46.4	621	46.7	0.98	382.6	3.81×10^{-6}	10.0
8	6	819	40.3	538	46.5	0.85	381.6	2.79×10^{-6}	8.7

The primary mechanism that drives FTV is the flow field that occurs near the injection slot. The FTV force mainly results from a local increase in surface pressure due to a separation in the boundary layer upstream of the injector induced by the interaction of the strong shock generated by the plume of injectant. This is shown schematically in Figure 21 for sidewall injection into the flow over a flat plate investigated by Spaid (1975). The size of this separation can be measured directly from the schlieren footage or from the processed PSP data. Figure 22 shows a schlieren image from the high-speed experimental video with the primary flow features identified. Similar features occur in each case.
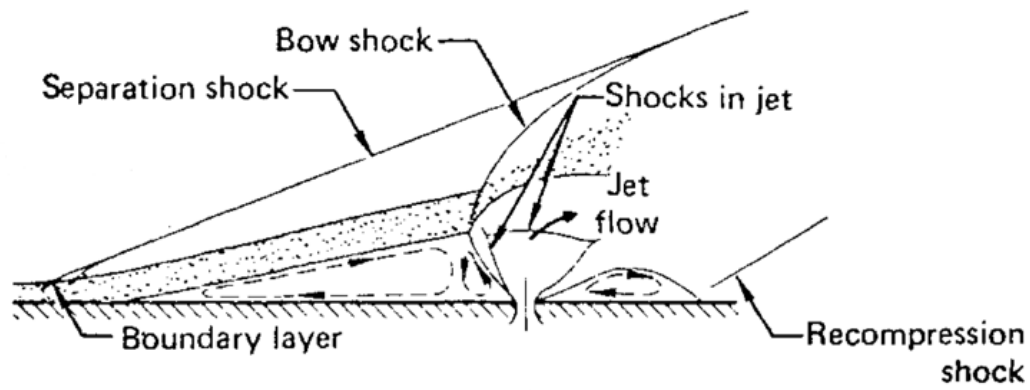
Figure 21. The theoretical flow field around a supersonic jet into a hypersonic crossflow, taken from Spaid (1975)
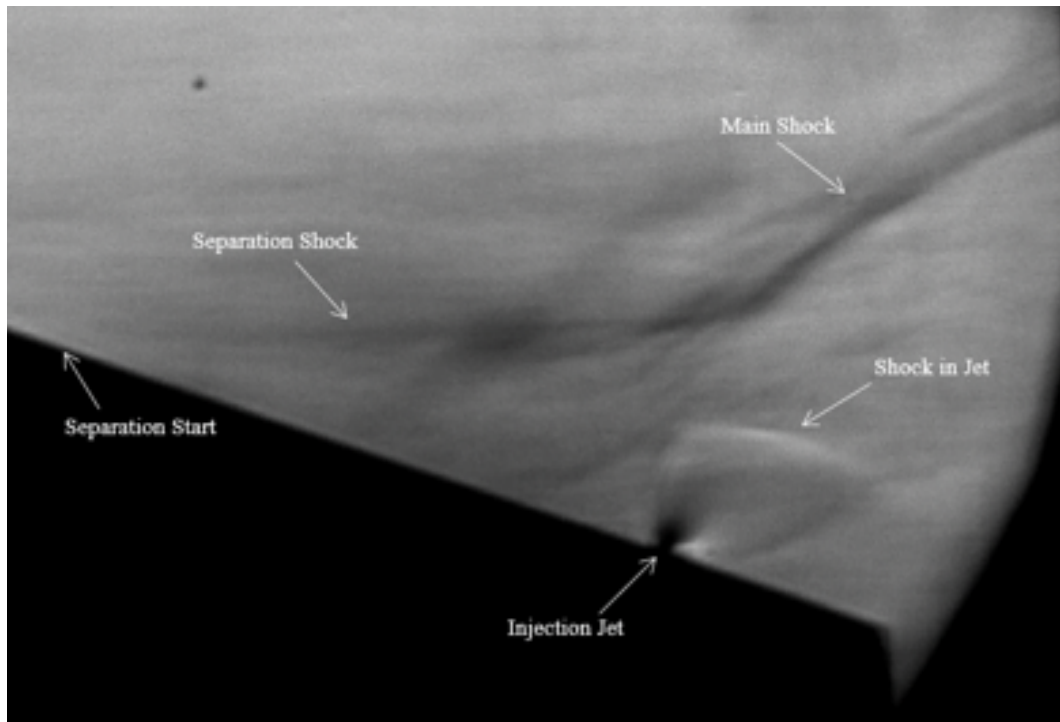

Figure 22. Schlieren image from the second plateau of a condition A shot with 120 kPa injection pressure showing the detail of the separation induced upstream of the injector plume.

At each freestream/injection condition, two repeat tests were undertaken with the injection gas being air and N_2. This allowed for the calculation of the local film effectiveness (Equation 1) from the PSP measurements. This gives a direct measurement of where the injection gas reaches and the separation distance.

$$\eta = 1 - \left(\left(\frac{p_{air}}{p_{NO_2}} - 1\right)\frac{M_{NO_2}}{M_{air}} + 1\right)$$ (1)

The film effectiveness on the exhaust, as defined by Equation 1, is presented for a single case in Figure 23. This shows that just upstream of the injector there is a high concentration of the injected gas in the separation region ranging from a film effectiveness of 0.3 to 0.7. On both spanwise edges, injectant is seen to be further upstream due to the lower pressure on either side due to three-dimensional spillage, thus allowing for an increased separation distance. Downstream of the injector, there is a near zero value of film effectiveness suggesting the injected gas completely lifts-off from the surface. There appears to be some artefact seen in the upstream location which should not be present and is likely an effect of non-ideal illumination of the PSP.

Figure 24 compares the separation distance determined from the PSP and schlieren imaging as a function of injection pressure ratio. The data agree extremely well. The separation distance is seen to rise rapidly for a small amount of injection, though the rise tails off at higher injection pressures. Lower Reynolds numbers have slightly larger separation

13

distances, which would not be expected for 2D flat plates (Kumar & Smith 1997). This suggests that the three dimensional geometry and presence of the pressure gradient due to the nozzle expansion must have an effect.
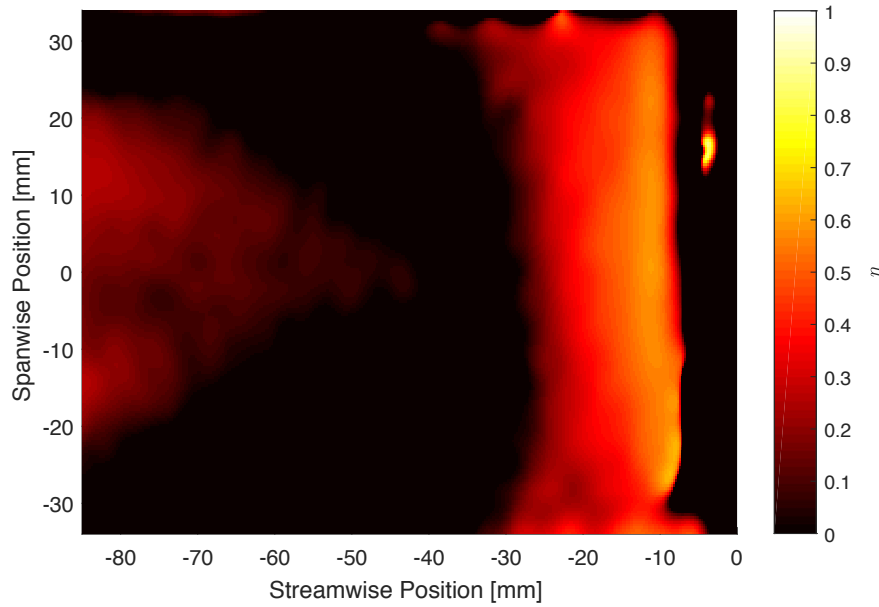

Figure 23. Film effectiveness map determined for unit Re = 21.7 ×10^6 m^{-1} and an injection pressure of 120 kPa.
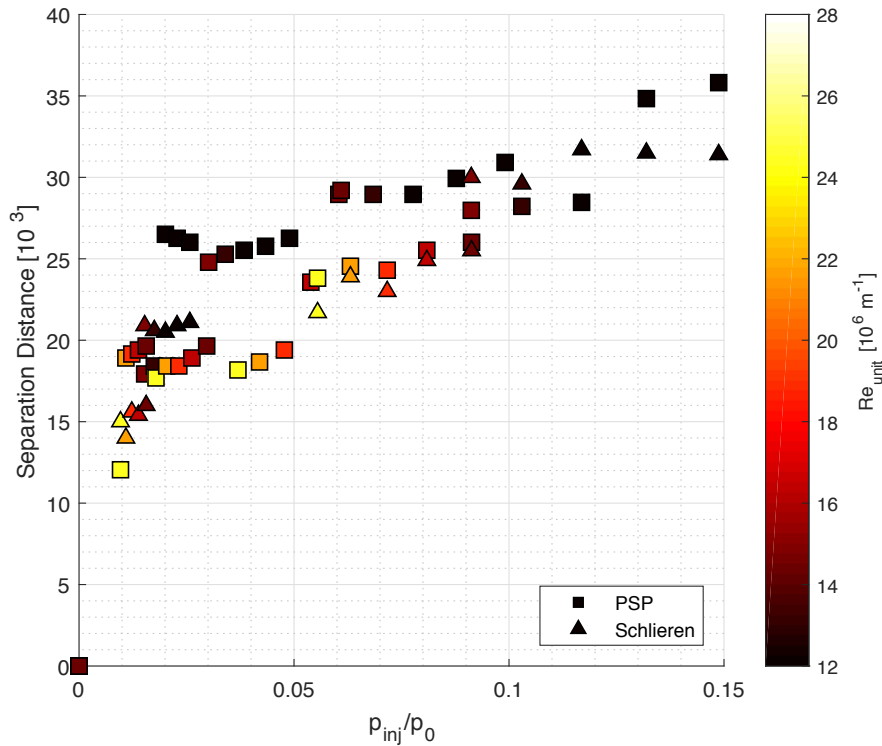

Figure 24. Comparison of the separation distances upstream of the injection location predicted by the 2D CFD simulations and measured in the experiments.

A comparison of the pressure distribution, measured by the PSP on the nozzle surface, with and without injection across the exhaust is presented in Figure 25. The injection case shows a significant increase in the pressure just upstream of the injector followed by a drop-off downstream. The three dimensional spillage is clearly visible, particularly in the injection case where it is more pronounced than the no-injection case. This is potentially due to the fact that the array of injector is not full width and thus neither is the full interaction of the cross flow with the injector plumes (see Figure 16).
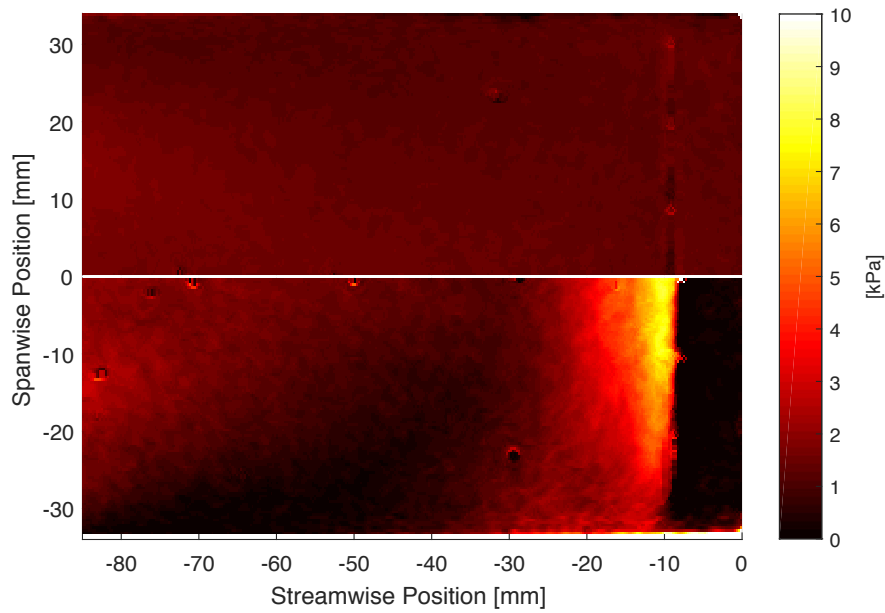
Figure 25. Surface pressure for a unit Re = 21.7 ×10⁶ m⁻¹ with no injection (top) and injection at 120 kPa (bottom).

Figure 26 shows the centreline pressure normalised by the no injection cases for different injection pressures for a freestream unit Reynolds number of 13.2 ×10⁶ m⁻¹. As injection pressure increases, a larger peak pressure is measured upstream of the injector and the separation length increases. The two dimensional CFD does not agree with the experiments, with a much lower peak normalised pressure and a larger separation distance including a shallower region.
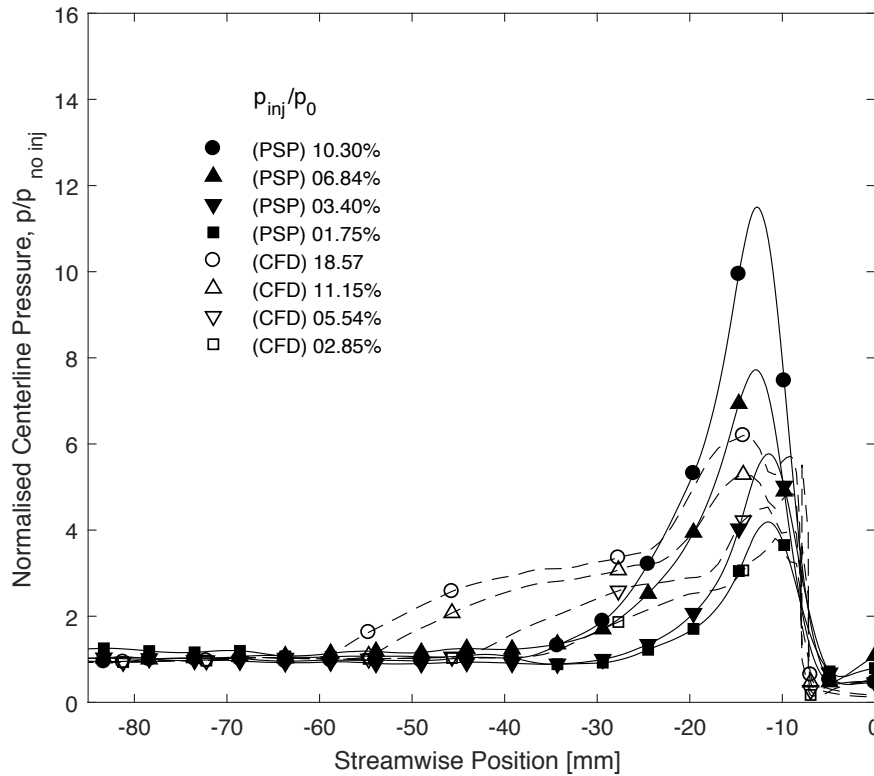

Figure 26. Surface pressure normalised by the corresponding no injection case, for a unit Re = 13.2 ×10⁶ m⁻¹ at various injection pressures.

To compare all of the tests, the moment and force ratios are defined in Equations 2, 3 and 4. Figures 27, 28, and 29 show these load ratios plotted against the injection pressure ratio. In each case, there is a strong linear relationship between the

plotted ratio and the injection pressure ratio. The results from CFD simulations are also presented for comparison, a very close agreement is seen in pitch and drag ratios. There is a clear discrepancy in the experimental and numerical lift ratio.

$$\text{Lift ratio} = \frac{L_{inj} - L_{no\ inj}}{L_{no\ inj}} \tag{2}$$

$$\text{Drag ratio} = \frac{D_{inj} - D_{no\ inj}}{D_{no\ inj}} \tag{3}$$

$$\text{Pitch moment ratio} = \frac{M_{inj} - M_{no\ inj}}{M_{no\ inj}} \tag{4}$$

In the experiments, the volume underneath the model protected by the shielding filled with gas and resulted in a significant static pressure to produce an additional lift force on the model. Due to this force being a distributed load it had a negligible effect on the pitch. This is not captured in the 2D simulations. The corrected CFD points in Figure 27 were created by adding an offset to the no-injection lift forces, representing this effect. The forces correspond to a pressure of approximately 1500 Pa and 2500 Pa for the 13 bar and 21.5 bar total pressure conditions respectively. This is approximately what would be expected and in the next test campaign a pressure transducer will be placed underneath the model to directly measure this effect. The points are coloured depending on the freestream Reynolds number of the shot. Data all lies close to the same line, suggesting a Reynolds number independence. This agrees well with the conclusions drawn by Spaid (1975).
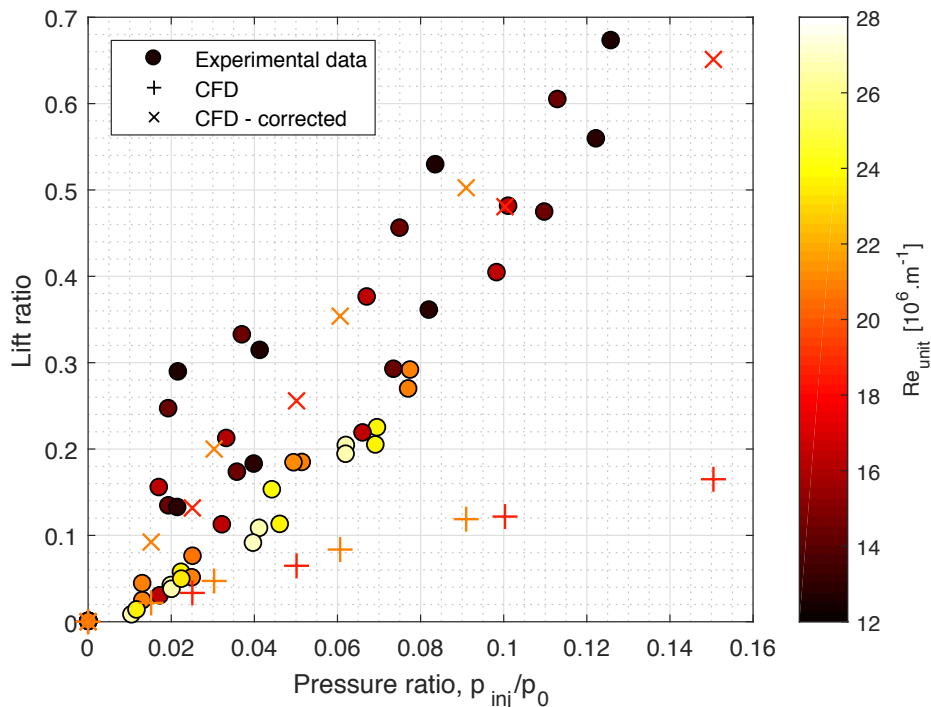

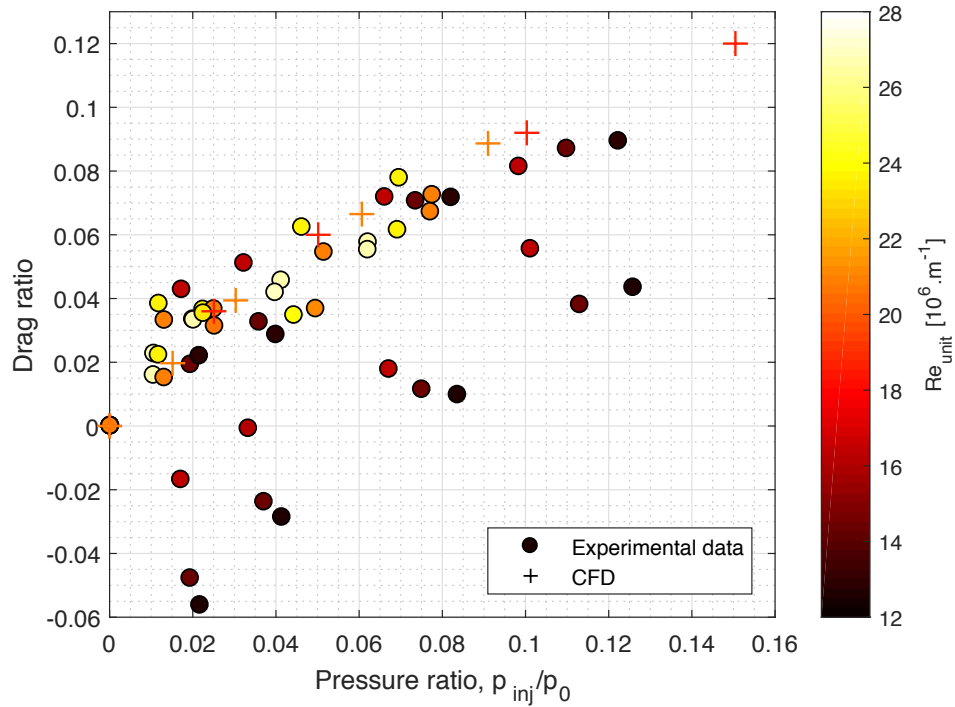Figure 27. The dependence of lift ratio (eq. 2) on pressure ratio.

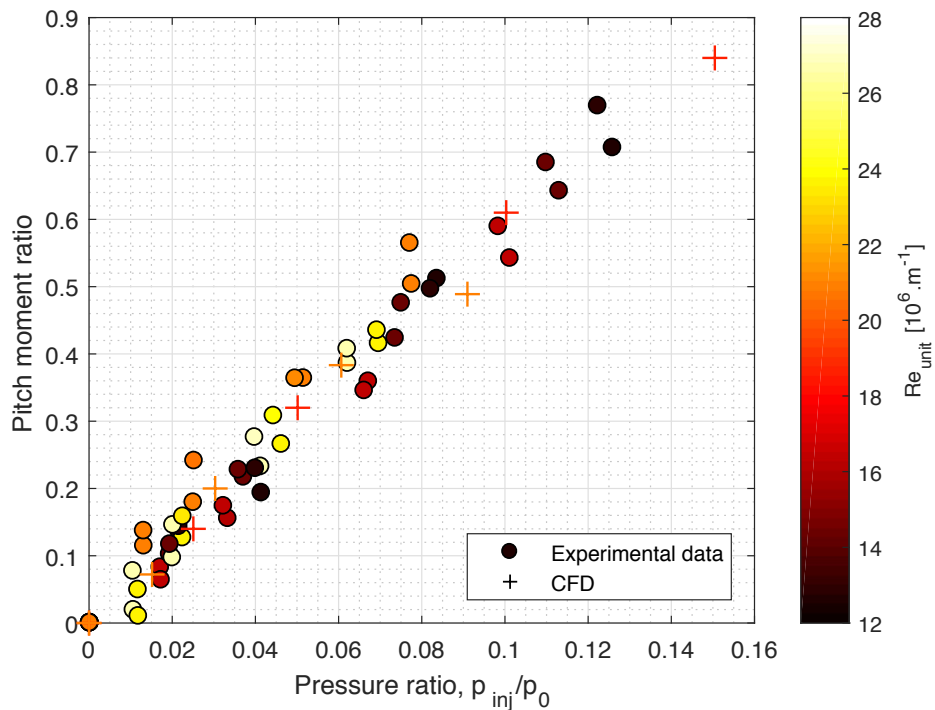Figure 28. The dependence of drag ratio (eq. 3) on pressure ratio.

Figure 29. The dependence of pitch moment ratio (eq. 4) on pressure ratio.

The interaction between a jet and a supersonic freestream is well understood for a parallel crossflow and the effectiveness of the jet can be described by an amplification factor, K. This is defined as the upstream interaction force plus the jet thrust normalised by the vacuum thrust of a sonic jet with the same total pressure and mass flow rate (Spaid 1975) (Equations 5, 6 and 7). For the experimental data, the upstream interaction force plus the jet thrust can be simplified as the difference between the lift and drag forces in the direction normal to the expansion surface of the model.

$$K = \frac{F_{inj} - F_{no\ inj}}{T_{vac}} \tag{5}$$

$$T_{vac} = \dot{m}_{inj} A^* + p^*_{inj} A_{eff} \tag{6}$$

$$A_{eff} = C_d A^* \tag{7}$$

Figure 30 shows the K factors for each shot plotted against the injection pressure normalised by the freestream stagnation pressure. There is a large spread of K at low injection pressures because the effective FTV forces are relatively much smaller than the total measured forces so the uncertainty of the K factor is amplified. The uncertainty of the load cell measurements is approximately 3 % and 2 % for drag and lift forces respectively. This corresponds to an uncertainty in the K factor of approximately 20 % at higher injection pressure ratios. Some of the conclusions of Spaid (1975) can be observed in the data obtained from this experiment: the amplification factor typically remains between 2 and 4; the amplification factor is insensitive to boundary layer edge Reynolds numbers; the amplification factor decreases at higher injection to boundary layer edge pressure ratios.
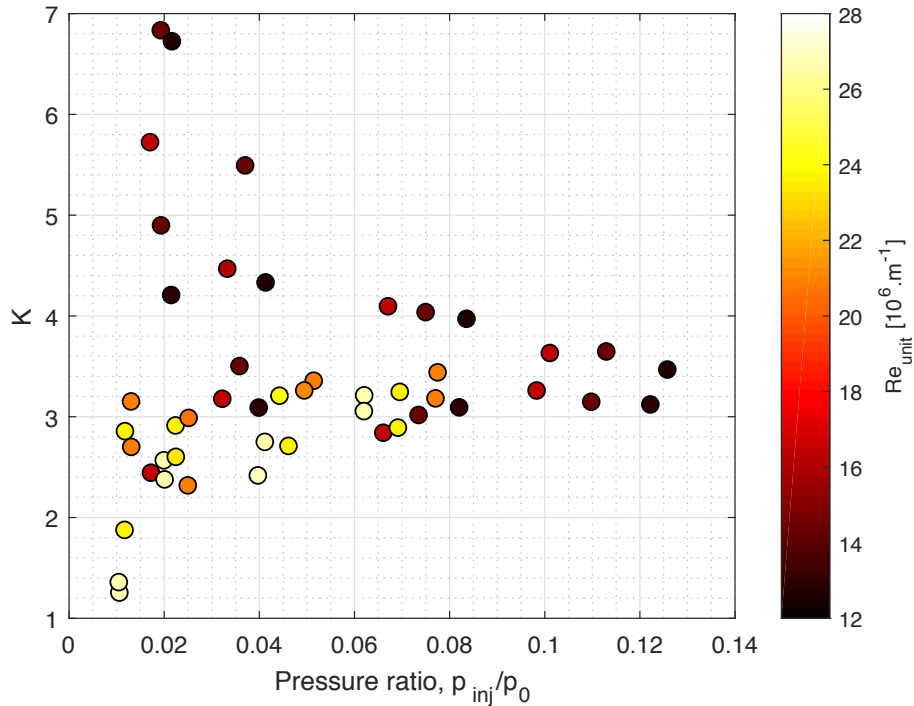

Figure 30. The dependence of amplification factor (eq. 5) on pressure ratio.

Conclusions

An experimental method integrating PSP, schlieren and a 6-component load cell for investigating fluidic thrust vectoring on hypersonic aircraft has been successfully demonstrated in the Oxford High Density Tunnel. Results obtained have been comparable to previous numerical and experimental research for a similar geometry and in more abstract studies. For a fundamental scramjet model, the forces produced by an FTV system have been found to be of a similar magnitude to the nominal, no injection, body forces. The ratios of the force components were found to have clear, proportionate relations to the injection pressure ratio. The amplification factor, K, was found to be of order 3, independent of Reynolds number and injection pressure ratio; in very good agreement with existing theory. 3D and spillage effects are noted to significantly affect the flow field. A strong relation between the size of the separated area and the FTV effect has been found. At low injection pressures, the incremental gain of additional injection is large, levering- off at higher injection pressures. Further investigation into alternative methods of increasing the size of the separation would are recommended.

The final phase of the project repeating the experiments for the internal expansion nozzle will be completed in early 2019.

Recommendations for Future Work

Now that the methodology for investigating the application of fluidic thrust vectoring in short duration hypersonic tunnels, has been successfully demonstrated, a number of recommendations are made to extend this work for hypersonic FTV including:

- Use a combination of CFD and experimental validation to investigate the vectoring performance of a range of injector locations.

- Use a combination of CFD and experimental validation to investigate the vectoring performance of a range of injector designs including arrays of sonic and supersonic porthole and slots.

- Use a combination of CFD and experimental validation to investigate the vectoring performance for a range of nozzle geometries.

- Design and test configurations that can vector in both pitch directions.

- Perform fundamental experiments to measure the interaction of an injector plume with expanding supersonic and hypersonic crossflows.

- Incorporate FTV into a pitching hypersonic model to measure control response.

Acknowledgements

References

1. Abdollahzadeh M, Rodrigues F, Pascoa J, Oliveira P (2015) Numerical design and analysis of a multi-DBD actuator configuration for the experimental testing of ACHEON nozzle model, *Aerospace Science and Technology*, 41, 259-273.

2. Ali A, Rodriguez C, Neely A, Young, J (2012) Combination of fluidic thrust modulation and vectoring in a 2D nozzle, 48th AIAA/ASME/SAE/ASEE Joint Propulsion Conference and Exhibit.

3. Berens T (1993) Numerical investigation of thrust vectoring by injection of secondary air into nozzle flows. In AGARD, Computational and Experimental Assessment of Jets in Cross Flow 15 p (SEE N94-28003 07-34).

4. Brandeis J, Gill J (1996) Experimental investigation of side-jet steering for supersonic and hypersonic missiles," Journal of Spacecraft and Rockets, 33(3), 346-352.

5. Brandeis J, Gill J (1998) Experimental investigation of super- and hypersonic jet interaction on missile configurations, *Journal of Spacecraft and Rockets*, 35(3), 296-302.

6. Bright C, Tuttle S, Neely A (2014) The effect of vacuum on shock vector control performance, Proceedings of the 19th Australasian Fluid Mechanics Conference, AFMC2014.

7. Deere K (2003) Summary of fluidic thrust vectoring research conducted at NASA Langley Research Center, The 21st AIAA Applied Aerodynamics Conference, 2003.

8. Gu R, Xu J, Mo J, Zhang K (2011) The Effect of Suction Tunnel Parameters on the Concordant Control of Inlet/SERN of the Off-design Scramjet, AIAA 2011-2331.

9. Hermann T, Ifti H, McGilvray M, Doherty L, Penty Geraets R (2018) Mixing Characteristics in a Hypersonic Flow around a Transpiration Cooled Flat Plate Model," HiSST: International Conference on High-Speed Vehicle Science Technology, 804.

10. Keyes FG (1952) The conductivity, viscosity, specific heat, and Prandtl numbers for thirteen gases. Tech. rep., Prog. Squid, M.I.T.

11. Kowal H (2002) Advances in thrust vectoring and the application of flow-control technology." *Canadian Aeronautics and Space Journal*, 48(2).

12. Kumar DSJ, Smith A (1997) Hypersonic jet control effectiveness, *Shock Waves*.

13. Macheret SO, Shneider MN, Miles RB (2004) Magnetohydrodynamic and electrohydrodynamic control of hypersonic flows of weakly ionized plasmas. *AIAA Journal*, 42(7), 1378-1387.

14. Martin C, Powers L (1981) Feasibility study of LITVC for shuttle SRB, NASA report.

15. McClinton C (2006) X-43-Scramjet Power Breaks the Hypersonic Barrier: Dryden Lectureship in Research for 2006,"44th AIAA Aerospace Sciences Meeting and Exhibit.

16. Mee D, Daniel WJT, Simmons JM (1996) Three-component force balance for flows of millisecond duration, *AIAA Journal*, 34(3):590–595.

17. Neely A, Gesto F, Young J (2017) Performance studies of shock vector control fluidic thrust vectoring, Collection of Technical Papers - 43rd AIAA/ASME/SAE/ASEE Joint Propulsion Conference, pp. 941 - 954.

18. Shneider MN, Macheret SO (2005) Hypersonic Aerodynamic Control and Thrust Vectoring by Nonequilibrium Cold-Air MHD Devices. In 43rd AIAA Aerospace Sciences Meeting and Exhibit (p. 979).

19. Skujins T, Cesnik C, Oppenheimer M, Doman D (2010) Canard Elevon Interactions on a Hypersonic Vehicle, *Journal of Spacecraft and Rockets*, 47(1), 90-100.

20. Spaid F (1975) Two-Dimensional Jet Interaction Studies at Large Values of Reynolds and Mach Numbers, *AIAA Journal*, 13(11), 1430-1434.

21. Van Pelt H (2018) Shock Vector Control applied to a Converging-Diverging Nozzle and a Hypersonic Vehicle, UNSW PhD Thesis.

22. Van Pelt H, Neely A, Young J (2015) A system study on fluidic thrust vectoring, 20th AIAA International Space Planes and Hypersonic Systems and Technologies Conference.

23. Van Pelt H, Neely A, Young J, De Baar J, (2017) A numerical study into hypersonic fluidic thrust vectoring, ISABE2017.

24. Van Wie D, Drewry D, King D, Hudson C (2004) The hypersonic environment: required operating conditions and design challenges, *Journal of Materials Science*, 39(19), 5915-5924.

25. Willert C, Stasicki B, Klinner J, Moessner S (2010) Pulsed operation of high-power light emitting diodes for imaging flow velocimetry, *Meas. Sci. Technol.* 21:075402 DOI:10.1088/0957-0233/21/7/075402

26. Wu JM, Chapkis RL, Mager A (1961) Approximate analysis of thrust vector control by fluid injection. *ARS Journal*, 31(12),1677-1685.

27. Yetter J (1995) Why do airlines want and use thrust reversers? A compilation of airline industry responses to a survey regarding the use of thrust reversers on commercial transport airplanes.

From:	Andrew Neely <a.neely@adfa.edu.au>
Sent:	Wednesday, January 2, 2019 23:09
To:	SMITH, DOUGLAS R CIV USAF AFMC AFOSR/IOE
Cc:	Matthew McGilvray
Subject:	[Non-DoD Source] Re: AFOSR Grant FA9550-17-1-0401 Final Performance Report due 29 DECEMBER 2018

Hi Doug

publications (so far) as follow

cheers

Andrew

1. Ivison W, Hambidge C, McGilvray M, Steuer D, Hermann T, Neely A (2019) Fundamental Experiments of Fluidic Thrust Vectoring for a Hypersonic Vehicle, AIAA-2019-1680 (to be presented at SciTech next week)
2. Ivison W (2018) Fluidic Thrust Vectoring for Hypersonic Vehicles, 4th Year Project Thesis, Department of Engineering Science, University of Oxford.
3. H. van Pelt, A.J. Neely and L.P. McQuellin, W. Ivison, M. McGilvray, C .Hambridge, T. Hermann, L. Doherty, D. Buttsworth, R. Choudhury (2019) Wind Tunnel Testing of Fluidic Thrust Vectoring in a Scramjet Nozzle, accepted for presentation at ISABE2019, Canberra, Australia, 23-27 September.

Andrew J Neely   BE, MEngSc, PhD (Qld), CEng, FRAeS, AFAIAA

Professor | School of Engineering & Information Technology
UNSW Canberra
Ph: +61 2 62688251 | Fax: +61 2 62688276 | email: a.neely@adfa.edu.au | web: seit.unsw.adfa.edu.au | location: Rm 361, Bldg 21
Web: research.unsw.edu.au/people/professor-andrew-james-neely

On 2 Jan 2019, at 9:40 pm, SMITH, DOUGLAS R CIV USAF AFMC AFOSR/IOE <douglas.smith.82@us.af.mil> wrote:

Dear Andrew & Matthew,